Title	Intra-tumoural heterogeneity characterization through texture and colour analysis for differentiation of non-small cell lung carcinoma subtypes
Authors	Ma, Yuan;Feng, Wei;Wu, Zhiyuan;Liu, Mengyang;Zhang, Feng;Liang, Zhigang;Cui, Chunlei;Huang, Jian;Li, Xia;Guo, Xiuhua
Publication date	2018-08-22
Original Citation	Ma, Y., Feng, W., Wu, Z., Liu, M., Zhang, F., Liang, Z., Cui, C., Huang, J., Li, X. and Guo, X. (2018) 'Intra-tumoural heterogeneity characterization through texture and colour analysis for differentiation of non-small cell lung carcinoma subtypes', Physics in Medicine & Biology, 63(16), 165018 (14 pp). doi: 10.1088/1361-6560/aad648
Type of publication	Article (peer-reviewed)
Link to publisher's version	https://iopscience.iop.org/article/10.1088/1361-6560/aad648 - 10.1088/1361-6560/aad648
Rights	© 2018 Institute of Physics and Engineering in Medicine. This is an author-created, un-copyedited version of an article accepted for publication in Physics in Medicine & Biology. The publisher is not responsible for any errors or omissions in this version of the manuscript or any version derived from it. The Version of Record is available online at https://doi.org/10.1088/1361-6560/aad648. As the Version of Record of this article has been published on a subscription basis, this Accepted Manuscript is be available for reuse under a CC BY-NC-ND 3.0 licence after a 12 month embargo period. - https://creativecommons.org/licences/by-nc-nd/3.0
Download date	2024-04-23 12:42:10
Item downloaded from	https://hdl.handle.net/10468/9665

University College Cork, Ireland
Coláiste na hOllscoile Corcaigh

Physics in Medicine and Biology

Intra-tumoral Heterogeneity Characterization through Texture and Color Analysis for Differentiation of Non-small Cell Lung Carcinoma Subtypes

To cite this article before publication: Yuan Ma *et al* 2018 *Phys. Med. Biol.* in press https://doi.org/10.1088/1361-6560/aad648

IOP Publishing Journal Title
Journal **XX** (XXXX) XXXXXX https://doi.org/XXXX/XXXX

Intra-tumoral Heterogeneity Characterization through Texture and Colour Analysis for Differentiation of Non-small Cell Lung Carcinoma Subtypes

Yuan Ma[1,2], Wei Feng[1,2], Zhiyuan Wu[1,2], Mengyang Liu[1,2], Feng Zhang[1,2], Zhigang Liang[3], Chunlei Cui[3], Jian Huang[4] , Xia Li[5], Xiuhua Guo[1,2*]

[1] School of Public Health, Capital Medical University, Beijing, China
[2] Beijing Key Laboratory of Epidemiology, Beijing, China
[3] Department of Nuclear Medicine, Xuanwu Hospital Capital Medical University, Beijing, China
[4] School of Mathematical Sciences, University College Cork, Cork, Ireland
[5] Department of Mathematics and Statistics, La Trobe University, Australia

E-mail: statguo@ccmu.edu.cn

Received xxxxxx
Accepted for publication xxxxxx
Published xxxxxx

Abstract

Radiomics has shown potential in disease diagnosis but the feasibility for non-small cell lung carcinoma (NSCLC) subtypes classification is unclear. This study aims to explore the diagnosis value of texture and colour features from Positron Emission Tomography Computed Tomography (PET-CT) images in differentiation of NSCLC subtypes: adenocarcinoma (ADC) and squamous cell carcinoma (SqCC). Two patient cohorts were retrospectively collected into a dataset of 341 FDG PET-CT images of NSCLC tumours (125 ADC, 174 SqCC and 42 cases with unknown subtype). Quantification of texture and colour features was performed using freehand region of interests. The relation between extracted features and commonly used parameters, such as age, gender, tumour size and standard uptake value (SUVmax), was explored. To classify NSCLC subtypes, Support Vector Machine (SVM) algorithm was applied on these features and the classification performance was evaluated by receiver operating characteristic (ROC) curve analysis. There was a significant difference between ADC and SqCC subtype in texture and colour features (P<0.05). It showed that imaging features were significantly correlated to both SUVmax and tumour diameter (P<0.05). When evaluating classification performance, features combining texture and colour got an AUC of 0.89 (95% CI, 0.78 to 1.00), colour features got an AUC of 0.85 (95% CI, 0.71 to 0.99) and texture features got an AUC of 0.68 (95% CI, 0.48 to 0.88). Delong's test showed that AUC for features combining texture and colour was higher than that for texture features only (P=0.010), but not significantly different from that for colour features only (P=0.328). HSV colour features got a similar performance to RGB colour features (P=0.473). The colour features are promising in the refinement of the NSCLC subtype differentiation and the features combining texture and colour of PET-CT images could result in better classification performance.

Keywords: Radiomics; Positron Emission Tomography Computed Tomography; Carcinoma, Non-Small-Cell Lung; Diagnostic Imaging; Colour

1. Introduction

Non-small cell lung carcinoma (NSCLC), the most common type of lung cancer, is one of serious diseases causing death for both men and women. NSCLC accounted for approximately 80-85% of lung cancer and the 5-year survival rate is less than 20% [1, 2]. NSCLC consists of two major histological subtypes: adenocarcinoma (ADC, 40-50%) and squamous cell carcinoma (SqCC, 20-30%). The two subtypes of NSCLC have their own tissue characteristics, anatomical location and glucose metabolism [3, 4], and it indicates that different optimal therapy strategies should be adopted respectively for the two subtypes of NSCLC to improve clinical outcomes. Before the establishment of targeted therapy, accurate histological subtype of tumours should be verified [5, 6]. In clinical, NSCLC subtypes are confirmed according to the histopathological analysis of tumour tissues by biopsy. However, these procedures are invasive and the risk in real practice can always exist. Other approaches using genomic and proteomic technologies have been developed, but these methods may be inefficient for tumour classification because of spatial and temporal heterogeneity of tumours [7]. Recently, radiomics has made up for these deficiencies mentioned above. Radiomics is a method that converts imaging data into a high dimensional feature space using a large number of automatically extracted data-characterization algorithms [8]. Different from the aforementioned approaches, radiomics is developed as prognostic or predictive biomarker to explore objective and precise quantitative imaging descriptors for disease classification and diagnosis [9].

With more advanced image capturing devices, more intuitive information could be obtained from medical images [10]. Multimodality images, including FDG PET-CT images that combine morphological information and metabolic information, can be a powerful tool in disease diagnosis based on radiomics[11]. Currently, there is an increasing interest in using FDG PET-CT images to quantify tumour tracer uptake heterogeneity and predict treatment outcomes [12, 13].

Texture features are the most frequently used radiomics that demonstrate association with many clinically relevant factors, like neoplasms histologic type[14,15], pathological stage[14,16], treatment prognosis[17] and prediction of tumor distant metastasis [18]. Wu [19] extracted 440 radiomic features, including tumour shape, tumour size, intensity statistics and texture features from CT images, and observed that 53 of them significantly correlated to tumour histology. Liu[20] found that CT pixel distribution and texture as appearing on CT images of peripheral lung adenocarcinomas can capture useful information regarding tumour phenotype.

Besides texture features, it is also possible to utilize colour information contained in images for disease diagnosis. Colour is the characteristic of human visual perception described through colour categories and can be quantified by different methods or colour spaces, similar to human colour perception. RGB colour space and HSV colour space are commonly used in image analysis. Studies have shown that good diagnosis results can be achieved by using colour features from RGB (Red, Green, Blue) or HSV (Hue, Saturation, Value) colour spaces[21,22]. David[23] extracted colour features from tongue images and described the relationship between tongue colour features and diseases. Fons can der Sommen[24] extracted texture and colour features from endoscopic images and verified the usefulness of colour features for early neoplasia detection in Barrett's esophagus. Therefore, as a non-invasive and cost-effective way for disease diagnosis and classification, radiomics, to some extent, is playing an important role in determining optimal treatment strategies and promoting the development of personalized medicine.

Studies on the association between radiomic features and diseases have been done [25, 26], but the clinical significance of radiomics for NSCLC histology subtypes classification is still unclear [13], especially with more advanced medical images, such as merged FDG PET-CT images. The study was done to explore the diagnosis value and clinical significance of texture and colour features from merged FDG PET-CT images in differentiation of NSCLC subtypes, namely ADC and SqCC, so that a high value to the medical decision-support could be made.

2. Materials and methods

2.1 Subjects and 18F-FDG PET-CT Imaging

Two patient cohorts were retrospectively collected into a data set of 341 merged FDG PET-CT images of NSCLC tumours, consisting of 125 ADC, 174 SqCC and 42 cases with unknown subtype. All slices containing nodule lesions of each tumor were used in the experiment and one slice was regarded as a case. Pathologic confirmation of tumour was done by surgical resection. The two cohorts were from Xuanwu Hospital Capital Medical University in China (140 images) and Cork University Hospital in Ireland (CUH) (201 images) from October 2012 to March 2016 respectively. In both cohorts, patients underwent clinical FDG PET-CT scanning prior to treatment. The CUH cohort was from a study reported by Nicola Marie Hughes and Wolsztynski et al. [27], which consider the use of PET for assessment of patient survival focusing on potential for enhanced staging of NSCLC patients. We used the 299 cases of confirmed histological subtype with their information such as age, gender and tumour size to assess the feasibility of texture and colour features in

discriminating NSCLC subtypes. The remaining 42 cases were used to explore the association between imaging features and traditional diagnostic factors such as tumour size, SUVmax (standard uptake value). All images in our study met the following criteria: the NSCLC was histologically confirmed; the lesions in images were of clear visibility. A sample of the merged PET-CT image enrolled in our study was shown in Figure 1.

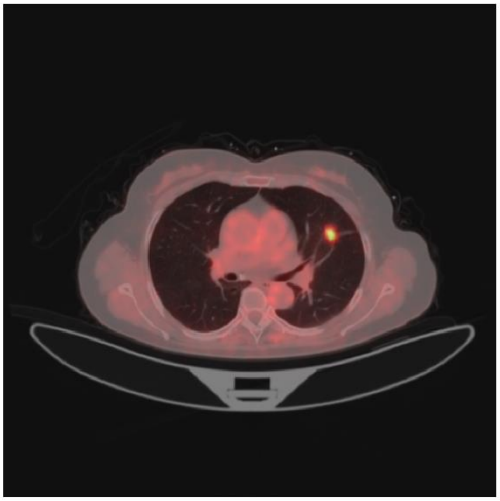

Figure 1 A sample of merged PET/CT image showing a cancerous tumor in the left lung

For each cohort, all acquisitions were based on the corresponding institutional protocols. Patients in Xuanwu Hospital Capital Medical University underwent whole body 18F-FDG PET-CT scan on a UNITED IMAGING uMI S-96R system after 6h of fasting time. Each patient was injected with FDG (range 3.70-5.56 Mbq/ kg) intravenously 60 minutes before the acquisition. CT data were acquired first (120 kV and 180 mA, no contrast enhancement) and PET images were subsequently reconstructed in the system using the ordered-subset expectation maximization (OSEM) algorithm with 3 iterations and a 3 mm full-width at half-maximum Gaussian post-filtering. The CT and PET images were systematically merged automatically in the system. All patients from Cork University Hospital underwent standard18F- FDG PET-CT scan on a GE Discovery VCT system following their institutional protocol. Low dose computed tomograghic scan was performed for attenuation correction of PET emission data. Subsequently, PET acquisition started with the delay time of 60 minutes from intravenous injection of 18F-FDG (range 340-400 Mbq). The CT and PET images were also systematically merged automatically in this system. The time delay between injection and acquisition was same for both of the two cohorts and it would not affect SUVmax related outcomes. The study was approved by the institutional review board in Xuanwu Hospital Capital Medical University. Informed consent was waived because of retrospective design of the study.

Images included into our study were collected from a UNITED IMAGING uMI S-96R system and a GE Discovery VCT system. A comparison experiment between the two sources of images would be performed to see if there is any significant difference on imaging features between them.

2.2 Image analysis

In our study, all image analysis were performed based on merged PET-CT images from the PET-CT acquisition. Texture analysis and colour analysis were adopted to quantify image features. First, image preprocessing was carried out. All lesions were delineated manually around cross-sectional area as region of interest (ROI) from merged PET-CT images by an experienced radiologist who was not blinded to the radiological findings and pathology. These hand-free ROIs were refined by avoiding necrosis, hemorrhage and cystic areas. After the image preprocessing was finished, quantification of texture and colour features was carried out. These extracted image features would be used to explore the correlation with other commonly used factors for tumour diagnosis, such as tumour size and SUVmax. Finally, support vector machine classifiers (SVM) would be built based on these image features to discriminate different subtypes of NSCLC. The pathology results were the golden standard for the classification. The image preprocessing and image feature extraction were implemented with Matlab software (The MathWorks, Natick, Massachusetts, Inc).

2.2.1 Texture features. In our study, texture features were calculated for ROIs from merged PET-CT images. Gray-level Co-occurrence matrix (GLCM) based texture parameters, which calculate how often a pixel of intensity i co-occur to another pixel of intensity j with pre-defined relationship of certain distance and direction [28], are commonly used in image analysis. In our study, GLCM was adopted to calculate texture parameters regarding four orientations (0 °, 45 °, 90 °, and 135 °) and distance of 1 pixel after images were quantized to 16 grey levels. The selected features were entropy, energy, inverse different moment (IDM) and correlation. All these features were the most representative and robust among all texture features [29]. The mean and standard deviation of the four features were calculated and finally eight texture features including entropy mean, entropy standard deviation, energy mean, energy standard deviation, IDM mean, IDM standard deviation, correlation mean, correlation standard deviation were adopted in our study. To improve our classification, the Gray-level Difference Statistics (GLDS) [30], the Gray-Gradient Co-occurrence Matrix (GGCM) [31] were also

calculated in our study in addition to GLCM. Mean, Entropy, Variance and Contrast were calculated by GLDS algorithm. From the GGCM, the following 15 features were included in our analysis: little gradient dominance, large gradient dominance, gray heterogeneity, gradient heterogeneity, energy, gray average, gradient average, gray mean square error, gradient mean square error, correlation, gray entropy, gray entropy, hybrid entropy, inertia and inverse difference moment. The classification performance of these texture features would be compared.

2.2.2 Colour features. Colour characteristics have been shown to significantly improve tumour classification and segmentation [32]. To acquire merged PET/CT images, the colour overlay technique was applied that the grayscale CT image and grayscale PET image are converted to colour images by colour table [33]. In our study, colour features were calculated for ROIs from merged PET-CT images. In this paper, we considered two colour spaces: RGB and HSV. RGB is the most popular colour representation, describing the red, green and blue intensity values in images [34]. In addition to RGB colour space, HSV colour space is also commonly used, representing colours by three channels of colour: hue (H), saturation (S) and value (V) [35]. The method of colour space conversion to HSV from RGB is described comprehensively in previous studies [36].

The mean and variance of an image of size $n * m$ are most commonly used features for RGB colour components defined as following equations [37], where X_{ij} is the pixel value of the i^{th} row and j^{th} column.

$$mean = \sum_{i=1}\sum_{j=1} X_{ij}/mn$$

$$variance = \frac{1}{nm}\sum_{i=1}^{n}\sum_{j=1}^{m}(X_{ij} - mean)^2$$

The colour histogram represents the colour distribution and forms the feature vectors for an image. Before the colour histogram is generated, the colour quantification need to be done. The colour space are divided into several small ranges and each interval is regarded as a bin. The colour histogram can be calculated through counting pixels in each bin.

To describe RGB colour characteristics, the colour characteristics of images were described by three colour histograms with 256 bins for R, G and B channels respectively. Colour features obtained for images included: average red, green and blue pixel (R, G and B) values, the variance of red, green and blue pixel (R, G and B) values.

In HSV colour space, H is an angle relative to Red axis varying between 0 °and 360 °, S is the depth or purity of the colour ranging from 0 to 1. V represents the brightness ranging from 0 to 1 [38, 39]. Unlike RGB colour analysis, the non-uniform quantization of colour channels was applied. The non-uniform quantization, dividing the colour space into the subordinate colour spaces with a non-uniform interval on the each axis constructing the colour space, can reflect well substantial characteristics of the colour space [40]. In our study, colour image was transformed from RGB space to HSV space at first and then non-uniform quantization of the H, S and V channels was made. The hue (H) channel was divided into 7 bins and the component range can be described as [0 °, 22 °] ∪ (330 °, 360 °], (22 °, 45 °], (45 °, 70°], (70 °, 155 °], (155 °, 186 °], (186 °, 278 °], (278 °, 330 °]. Saturation (S) was divided into 2 bins and the component range can be described as [0, 0.65], (0.65, 1]. The brightness (V) was divided into 2 bins with component ranges [0, 0.5] and (0.5, 1]. According to the above quantization, the 3 colour components (H, S, and V) were combined into one dimensional feature vector [41]: $L = HQ_SQ_V + SQ_S + V$, where Q_S and Q_V were the quantization divisions of S and V components. The final feature vector could be described as: $L = 4 * H + 2 * S + V$. According to this equation, the vector L ranged from 0 to 27. Hence, the one-dimensional histogram with 28 bins was obtained. These 28 pixel frequencies were adopted as HSV colour features after normalization.

2.3 Statistical analysis

First, the comparison experiment between GE and United images was performed to compare if there were significant difference of texture and colour features between these two machines from two cohorts in our study. Data mining method: PCA (Principal Component Analysis) was applied to make the comparison. The PCA score plots were drawn to compare these two machines. The statistical difference of components was explored by a two-sided Wilcoxon rank-sum test.

For descriptive analysis, texture features and RGB colour features were expressed as mean ± SD; HSV colour features were reported as median (P25-P75). Categorical variables were provided as frequencies (percentage). A two-sided Wilcoxon rank-sum test was applied to make a comparison between ADC and SqCC on image features. Correlations between imaging features and other radiomic features such as SUVmax, tumour size, were evaluated using Spearman rho. For visualizing the pairwise correlation between image features, as well as its relationship to other radiomic features, heatmap was generated. A *P* value of 0.05 was regarded as a threshold for a certain statistical significance.

Discriminatory analysis was conducted using a machine learning algorithm called Support Vector Machine (SVM) to evaluate the predictive ability for cancer subtypes. The Radial Basis Function (RBF) kernel was used because of its better performance than other less complex linear functions

[32, 42]. The classification error was estimated using ten fold cross validation method by dividing the data into ten, nine for training and one for testing. The models with the best test accuracy was selected by applying ten-fold cross validation method ten times.

The detection performance of our models were then evaluated for testing data and whole dataset by ROC analysis respectively. The ROC curve was created by plotting the true positive rate (TPR) against the false positive rate (FPR) at various threshold settings. The TPR defined how many correct positive results occur among all positive samples available during the test. FPR defined how many incorrect positive results occur among all negative samples available during the test. In ROC analysis, the pathological result of NSCLC subtypes was taken as the dependent factor, and the positive predictive probability calculated from SVM classifiers was used to predict NSCLC subtypes.

All statistical analyses in our study were done with SAS version 9.4 (SAS Institute Inc). The heatmap was generated using 'heatmap.2' function in 'gplots' package by R software (http://www.r- project.org/). The SVM algorithm and ROC analysis were implemented with 'e1071' package and 'pROC' package in R software respectively.

3. Results

3.1 Comparison between the two sources of imaging

The difference of imaging features between the two machines was explored for ADC subtype and SqCC subtype separately. The cumulative proportion of the first two components is 52.63% and 54.71% for ADC and SqCC respectively. The cumulative proportion of the first three components is 60.79% and 62.29% for ADC and SqCC respectively. The cumulative proportion of the first twenty-five components can reach over 99% for both ADC (99.39%) and SqCC (99.01%).

The two dimensional PCA score plots were drawn using the first two components. To compare more intuitively, the three dimensional PCA score plots were drawn by using the first three components. The smaller the spatial distribution difference, the more similar the data is. From Figure 2 (a), Figure 2 (b), we can see that there are many dots overlapped for the two machines, which means that there is no significant difference between the two machines. The statistical difference for these components calculated from PCA was explored by Wilcoxon rank-sum test (Table1). It can be seen that most components have no significant difference between the two machines ($P<0.05$).

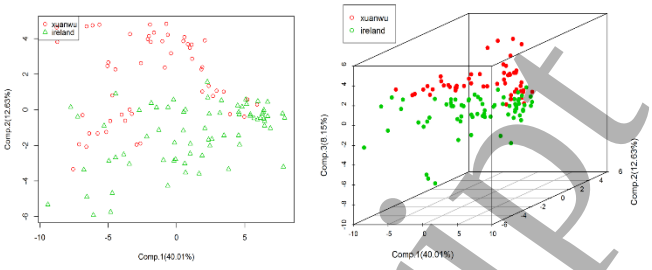

Figure 2 (a) The PCA score plots of imaging features for ADC in two machines

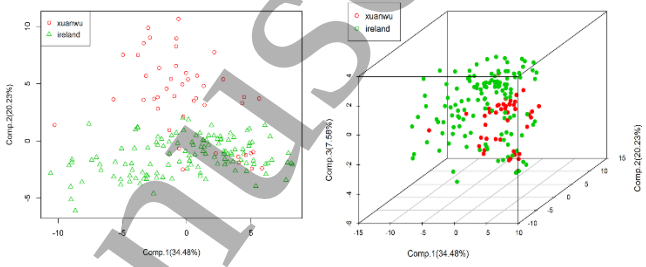

Figure 2 (b) The PCA score plots of imaging features for SqCC in two machines

Table 1 Comparison of Feature Components of the Two Machines for ADC and SqCC

	ADC		SqCC	
	Z	*P*	Z	*P*
Comp.1	-4.131	0.000*	-0.211	0.833
Comp.2	-6.410	0.000*	-7.491	0.000*
Comp.3	-5.056	0.000*	-6.188	0.000*
Comp.4	-2.758	0.006*	-2.377	0.017*
Comp.5	-0.540	0.590	-2.562	0.010*
Comp.6	-0.609	0.542	-0.026	0.979
Comp.7	-1.848	0.065	-0.913	0.362
Comp.8	-0.050	0.960	-0.545	0.586
Comp.9	-3.062	0.002*	-1.122	0.262
Comp.10	-3.912	0.000*	-0.438	0.661
Comp.11	-1.709	0.088	-0.070	0.944
Comp.12	-0.270	0.787	-1.236	0.217
Comp.13	-0.340	0.734	-1.077	0.281
Comp.14	-1.609	0.108	-0.153	0.878
Comp.15	-1.234	0.217	-1.005	0.315

Comp.16	-0.315	0.753	-0.655	0.513
Comp.17	-0.250	0.803	-2.243	0.025
Comp.18	-0.145	0.885	-0.411	0.681
Comp.19	-1.019	0.308	-0.229	0.819
Comp.20	-0.599	0.549	-0.232	0.817
Comp.21	-2.278	0.023*	-0.950	0.342
Comp.22	-0.250	0.803	-0.734	0.463
Comp.23	-1.289	0.197	-0.610	0.542
Comp.24	-0.984	0.325	-0.150	0.881
Comp.25	-0.155	0.877	-1.160	0.246

3.2 Characteristic description of NSCLC cases

Among the 341 cases (age, 68.44 ±9.51 years; male, 244 (71.55%)) included, there were 125 ADC cases, 174 SqCC cases and 42 cases with unknown subtype. The tumour size of ADC was 2.53±1.23 cm (range, 1.80~ 3.00 cm), tumour size of SqCC was 4.21±1.72 cm (range, 3.00~5.00 cm) and unknown subtype was 2.92 ±1.60 cm (range, 1.80~ 3.55 cm). Comparison between ADC and SqCC groups was done and there was a significant difference for age, gender and tumour size between the two groups (P<0.05) as was showed in Table 2.

Table 2 Characteristic Description of NSCLC Cases

	Overall (N=341)	ADC (N=125)	SqCC (N=174)	Unknown (N=42)	Z or χ^2 [a]	*P*
Age [b] (years)	68.44 ±9.51	70.36 ±8.93	67.68 ±9.94	65.91 ±8.46	2.415	0.016*
Gender n (%)					16.050	<0.0001*
Male	244 (71.55)	75 (60.00)	141 (81.03)	28 (66.67)		
Female	97 (28.45)	50 (40.00)	33 (18.97)	14 (33.33)		
Tumour size [b] (cm)						
mean ± SD	3.03 ±1.58	2.53 ±1.23	4.21 ±1.72	2.92 ±1.60	2.586	0.010*
median (P25-P75)	2.80(1.80~3.60)	2.55(1.80~3.00)	4.00(3.00~5.00)	2.70(1.80~3.55)		
SUVmax [b](g/ml)	-	-	-	8.57 ±4.46	-	-

[a] Age and tumour size comparison between ADC and SqCC groups were conducted by Wilcoxon rank-sum test and gender comparison was done by chi-square test.
[b] Age, Gender and Tumour size (centimeter) were described as mean ±SD.
* P<0.05, statistical significantly different between ADC and SqCC.

3.3 Comparison between image features of ADC and SqCC

To find out that whether there was a significant difference between the two subtypes of NSCLC in texture and colour features, comparison was carried out between ADC and SqCC. There was a significant difference between ADC and SqCC on image features as shown in Table 3, including 2 GLCM texture features (energy mean, Z=2.078, P=0.037; IDM standard deviation, Z=3.139, P=0.002), 8 GGCM texture features (P<0.05, respectively) and 6 colour features from HSV space (P<0.05, respectively). The colour histograms of the red, green and blue colour components were plotted respectively in Figure 3 to describe colour distribution in ADC and SqCC. The histograms showed that the red, green and blue colour components were more concentrated on lower pixel levels for ADC while they were more concentrated on higher pixel levels for SqCC, but the mean and variance of these three colour components did not show significant difference between ADC and SqCC (Table 3).

3.4 Selection of texture features

To select texture features, Support Vector Machine classifiers were built for GLCM features, GLDS features, GGCM features and GLCM+GLDS+GGCM features respectively. The ten-fold cross validation method was

applied to validate the models. The performance of these four classifiers for one-fold test dataset were shown in Table 4.

It showed that the best performance was obtained by GLCM texture features with an accuracy of 76.00%, AUC of 0.76 (95% CI, 0.56-0.95). The classification result got worse when all texture features were included into the experiment by Delong's test (D=-2.61, *P*=0.014). The GLDS features seemed to have a good performance, so another model established by combining GLCM and GLDS features was also established. This model got an accuracy of 67.00% and AUC of 0.54 (95% CI, 0.30-0.77) with no significant difference with the GLCM model (D=1.45, *P*=0.148).

Considering the classification performance and overfitting, only GLCM features were applied to the following analysis.

Table 3 Comparison of Image Features between Histological Subtypes

	ADC (N=125)	SqCC (N=174)	Z	*P*
energy_mean [a]	0.70±0.19	0.66±0.17	2.08	0.038*
energy_std [a]	0.009±0.004	0.010±0.004	-0.48	0.633
entropy_mean	0.77±0.42	0.83±0.37	-1.65	0.100
entropy_std	0.036±0.016	0.038±0.018	-0.77	0.441
IDM_mean	-28.28±78.93	-30.61±85.59	-1.76	0.079
IDM_std	0.48±2.12	0.37±1.26	3.14	0.002*
correlation_mean	0.95±0.03	0.95±0.02	0.83	0.409
correlation_std	0.010±0.005	0.011±0.005	-0.69	0.489
Mean	0.04±0.02	0.04±0.02	-0.98	0.329
Contrast	1792.49±770.56	1869.89±780.22	-0.74	0.459
Variance	0.71±0.18	0.68±0.16	1.88	0.060
Entropy	1.28±0.69	1.40±0.62	-1.75	0.082
Little gradient dominance	0.88±0.08	0.87±0.08	1.49	0.137
Large gradient dominance	1.62±0.85	1.66±0.82	-0.61	0.543
Gray heterogeneity	1405.28±994.57	1688.80±953.44	-3.23	0.0013*
Gradient heterogeneity	1617.06±1215.51	2083.54±1589.35	-3.54	0.0004*
Energy	0.67±0.21	0.62±0.19	2.15	0.032*
Gray average	28.51±23.62	33.81±23.27	-2.66	0.008*
Gradient average	1.62±0.85	1.66±0.82	-0.61	0.543
Gray mean square error	57.83±22.23	63.97±23.01	-2.56	0.010*
Gradient mean square error	5.50±1.25	5.54±2.21	-0.36	0.716
Correlation	91.37±44.53	88.76±45.00	0.49	0.621
Gray entropy	0.43±0.28	0.48±0.25	-1.89	0.059
Gradient entropy	0.28±0.16	0.31±0.14	-1.54	0.123

Hybrid entropy	0.59 ±0.39	0.64 ±0.35	-2.01	0.044*
Inertia	4938.41 ±5117.70	6033.41 ±5283.75	-2.61	0.009*
Inverse difference moment	0.80 ±0.14	0.77 ±0.13	2.16	0.031*
red_mean [b]	64.98 ±41.10	69.57 ±48.18	-0.66	0.513
red_var [b]	46.15 ±25.10	49.64 ±23.14	-1.18	0.239
green_mean	83.88 ±41.99	90.17 ±50.75	-0.44	0.659
green_var	56.63 ±21.24	56.35 ±20.64	0.11	0.915
blue_mean	135.75 ±35.32	134.79 ±41.01	0.96	0.337
blue_var	49.62 ±18.27	52.01 ±19.77	-1.49	0.137
Feature1[c]	0.000 (0.000-0.003)	0.0002(0.0000-0.0032)	-1.23	0.220
Feature2	0.00 (0.0000-0.12)	0.0000 (0.0000-0.0006)	0.97	0.330
Feature3	0.00 (0.00-0.00)	0.00 (0.00-0.00)	-0.36	0.716
Feature4	0.000 (0.000-0.001)	0.000 (0.000-0.006)	-2.46	0.014*
Feature5	0.00 (0.000-0.05)	0.000 (0.000-0.008)	1.27	0.203
Feature7	0.04 (0.00-0.12)	0.09 (0.00-0.15)	-2.52	0.012*
Feature9	0.000 (0.000-0.002)	0.000 (0.000-0.003)	-1.13	0.258
Feature10	0.00 (0.00-0.00)	0.00 (0.00-0.00)	-0.84	0.401
Feature11	0.00 (0.00-0.07)	0.03 (0.00-0.11)	-3.55	0.0004*
Feature12	0.00 (0.00-0.03)	0.00 (0.00-0.02)	-0.51	0.610
Feature13	0.00 (0.00-0.06)	0.02 (0.00-0.07)	-2.23	0.026*
Feature17	0.00 (0.00-0.00)	0.0000 (0.0000-0.0003)	-2.11	0.035*
Feature18	0.00 (0.00-0.00)	0.00 (0.00-0.00)	-1.18	0.237
Feature19	0.00 (0.00-0.00)	0.00 (0.00-0.00)	0.98	0.326
Feature20	0	0.00 (0.00-0.00)	-0.84	0.401
Feature21	0.000 (0.000-0.003)	0.0002(0.0000-0.0032)	-1.23	0.220
Feature26	0.00 (0.0000-0.12)	0.0000 (0.0000-0.0006)	0.97	0.330
Feature27	0.00 (0.00-0.00)	0.00 (0.00-0.00)	-0.36	0.716
Feature28	0.000 (0.000-0.001)	0.000 (0.000-0.006)	-2.46	0.014*

[a] energy_mean refers to the mean of energy, energy_std means standard deviation of energy, the same for other texture features.

[b] red_mean refers to the mean of pixel counts for red channel, red_var means the variance of pixel counts for red channel, the same for the other two channels.

[c] Feature1- Feature28 refers to the normalized pixel counts for 28 bins of the HSV feature vector histogram respectively.

* $P<0.05$, statistically significant.

Feature6, feature8, feature14-16, feature22-25 in HSV features were deleted because their values were all 0.00 for all cases.

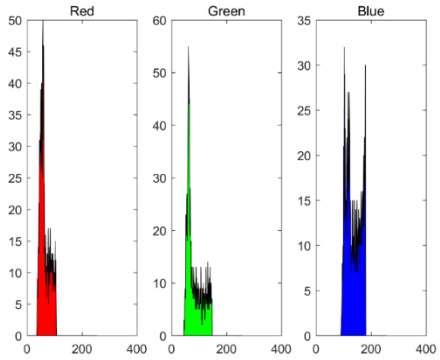

Figure 3 (a) The average colour histogram of the R, G and B components of 125 ADC images

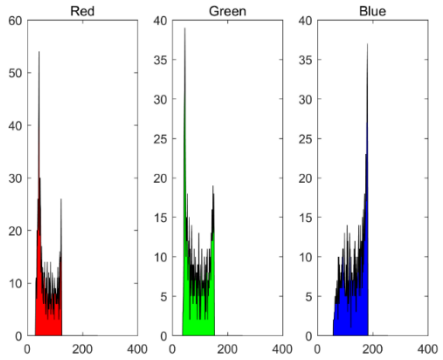

Figure 3 (b) The average colour histogram of the R, G and B components of 174 SqCC images.

Table 4 Evaluation of Classification Performance with Different Features on Test Data

Feature	Acc (%)	AUC (95% CI)	Thr*	Sen*	Spe*
GLCM	0.76	0.76 (0.56-0.95)	0.54	0.83	0.75
GLDS	0.61	0.53 (0.30-0.76)	0.61	1.00	0.17
GGCM	0.60	0.50 (0.50-0.50)	-	1.00	0.00
GLCM+ GLDS	0.67	0.54 (0.30-0.77)	0.57	0.52	0.67
All texture	0.60	0.50 (0.50-0.50)	-	1.00	0.00

*Thre means threshold, Sen means Sensitivity and Spe means Specificity.

3.5 Pairwise correlation between imaging features, as well as other traditional radiomic features

To explore the pairwise correlation between imaging features, heatmap was plotted in Figure 4. The relation between imaging features and other two factors (SUVmax, tumour size) that were always taken into account when radiologists make the diagnosis[43] were also shown in Figure 3. We can see that most of the features associated with each other. To determine the significance of correlation between imaging features and the two traditional radiomic features, the Spearman's ρ correlation coefficients were computed. As the Table 5 shown, there were 12 imaging features correlated to SUVmax significantly (P<0.05, respectively), with |ρ| ranging from 0.307 to 0.528. There were 12 imaging features correlated to tumour size (P<0.05, respectively), with |ρ| ranging from 0.312 to 0.412. The 2 GLCM texture features and 6 HSV color features that had significant difference between ADC and SqCC shown in Table 3 were correlated to SUVmax or tumour size significantly. Among the 17 features showing significantly association with SUVmax or tumour size, 7 features appeared as significantly correlated to both of them, including 3 texture features (energy mean, IDM mean, IDM standard deviation) and 4 colour features (red mean, green mean and 2 HSV colour features).

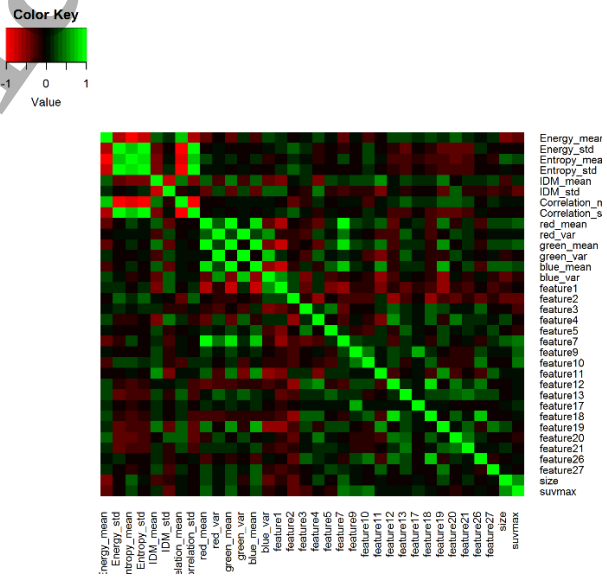

Figure 4 Pairwise correlation between imaging features, as well as its relationship to SUVmax and tumor size

Table 5 Correlation between Image Features and SUVmax, Tumour Size

Image features	Correlation to SUV_{max}		Correlation to tumour diameter	
	ρ	*P*	ρ	*P*
energy_mean [a]	-0.325	0.036*	-0.357	0.020*
energy_std	-0.041	0.796	-0.135	0.394
entropy_mean	0.190	0.229	0.239	0.127
entropy_std	-0.019	0.904	-0.003	0.987
IDM_mean	0.511	0.001*	0.312	0.045*
IDM_std	-0.469	0.002*	-0.329	0.033*
correlation_mean	0.071	0.655	0.089	0.575
correlation_std	-0.035	0.825	-0.092	0.561
red_mean [b]	0.354	0.021*	0.336	0.029*
red_var	0.009	0.957	-0.159	0.315
green_mean	0.357	0.020*	0.372	0.015*
green_var	-0.010	0.949	-0.156	0.322
blue_mean	0.220	0.161	0.376	0.014*
blue_var	-0.096	0.545	-0.263	0.093
Feature1[c]	-0.138	0.382	-0.331	0.033*
Feature2	-0.314	0.043*	-0.351	0.022*
Feature3	-0.149	0.345	0.095	0.551
Feature4	0.094	0.552	0.075	0.635
Feature5	-0.141	0.374	0.117	0.459
Feature7	0.470	0.002*	0.332	0.032*
Feature9	0.375	0.014*	0.164	0.300
Feature10	0.528	0.000*	0.167	0.290
Feature11	0.167	0.291	0.283	0.069
Feature12	0.307	0.048*	0.242	0.123
Feature13	0.203	0.197	0.181	0.253
Feature17	0.258	0.099	0.168	0.288
Feature18	0.383	0.012*	0.198	0.209
Feature19	0.106	0.505	0.358	0.020*
Feature20	0.069	0.663	0.147	0.351

Feature21	0.132	0.404	0.354	0.021*
Feature26	0.310	0.046*	0.145	0.359
Feature27	0.212	0.177	0.412	0.007*
Feature28	0.110	0.490	0.226	0.151

[a] energy_mean refers to the mean of energy, energy_std means standard deviation of energy, the same for other texture features.

[b] red_mean refers to the mean of pixel counts for red channel, red_var means the variance of pixel counts for red channel, the same for the other two channels.

[c] Feature1- Feature28 refers to the normalized pixel counts for 28 bins of the HSV feature vector histogram respectively.

* P<0.05, statistically significant.

Feature6, feature8, feature14-16, feature22-25 in HSV features were deleted because their values were all 0.00 for all cases.

3.6 Classification performance

To classify NSCLC subtypes, Support Vector Machine classifiers were built for features combining texture (GLCM texture features) and colour features (RGB+HSV), only texture features, only colour features respectively with confirmed pathological result as golden standard. The model with the best test accuracy was selected by applying ten-fold cross validation method ten times. The classification performance of these models for testing data by ROC analysis was shown in Table 6. From Table 6, we can see that the best classification performance for test dataset was obtained by using features combining texture and colour with accuracy of 80.00%, AUC of 0.89 (95% CI, 0.78 to 1.00), sensitivity of 0.73 and specificity of 1.00. When only the colour features (RGB+HSV) were applied for classification, we got the accuracy of 70.00%, AUC of 0.85 (95% CI, 0.71 to 0.99), sensitivity of 0.77 and specificity of 1.00. When only GLCM texture features were applied, we got the accuracy of 70.00%, AUC of 0.68 (95% CI, 0.48 to 0.88), sensitivity of 0.36 and specificity of 1.00. Delong's test for ROC curves comparison was done and it was found that the AUC for features combining texture and colour was higher than that for texture features only (Z=2.57, P= 0.010), but not significantly different from that for colour features only (Z=0.98, P= 0.328). HSV colour features (AUC, 0.64; 95%CI, 0.36 to 0.91) got a similar performance to RGB colour features (AUC, 0.52; 95% CI, 0.28 to 0.77) (P=0.450).

The models were also applied on our whole dataset. The classification performance was shown in Table 7. The ROC curves using all the data were drawn on Figure 5 and Figure 6. It was found that the classification performance based on all the data was better than that based on test dataset and there was a significant difference between the AUC of RGB color and AUC of HSV color. The cut-off value threshold(s) corresponding to the best sum of sensitivity+ specificity was adopted.

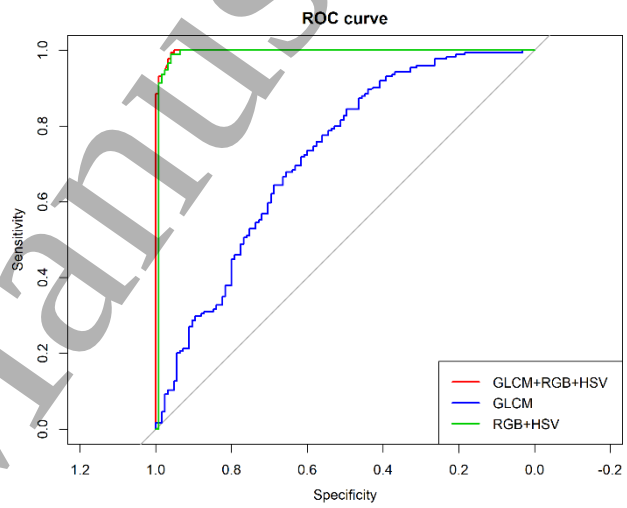

Figure 5 ROC curves of classification results with texture or colour parameters.

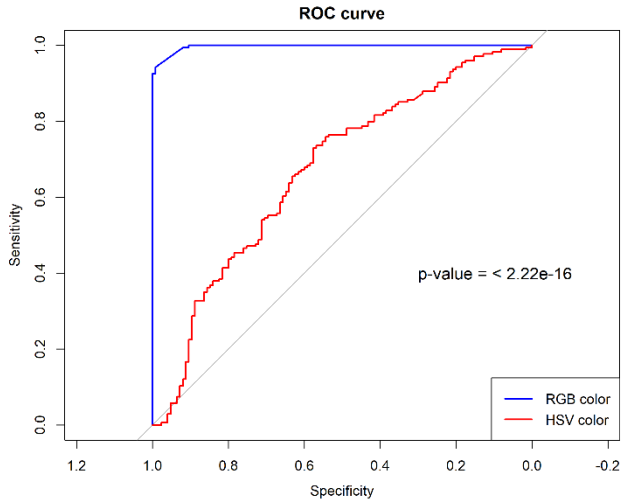

Figure 6 AUC comparison between RGB and HSV colour

Table 6 Evaluation of Classification Performance with Different Features on One-fold Test Dataset

Feature	Accuracy (%)	AUC (95% CI)	Threshold	Sensitivity	Specificity
GLCM +RGB+HSV	80.00	0.89 (0.78-1.00)	0.55	0.73	1.00
RGB+HSV	70.00	0.85 (0.71-0.99)	0.56	0.77	1.00
GLCM	70.00	0.68 (0.48-0.88)	0.63	0.36	1.00
HSV	70.00	0.64 (0.36-0.91)	0.58	0.68	0.75
RGB	73.33	0.52 (0.28-0.77)	0.57	0.86	0.25

Table 7 Evaluation of Classification Performance with Different Features on Whole Dataset

Feature	Accuracy (%)	AUC (95% CI)	Threshold	Sensitivity	Specificity
GLCM +RGB+HSV	98.00	1.00 (0.99-1.00)	0.50	0.99	0.96
RGB+HSV	97.00	0.99 (0.97-1.00)	0.57	0.99	0.96
GLCM	70.00	0.72 (0.66-0.78)	0.60	0.84	0.50
HSV	63.00	0.67 (0.61-0.73)	0.58	0.73	0.58
RGB	96.00	1.00 (0.99-1.00)	0.58	0.94	0.99

4. Discussion

Personalized medicine, providing optimal treatment for an individual patient to promote health and to prolong the lifetime, has been capturing more and more attention in medical field [44]. However, the establishment of targeted therapy usually depends on confirmed histological subtypes of tumours by biopsy [7]. To avoid the risk in real practice of these invasive procedures, new approaches should be developed. Related studies have shown that SUVmax is correlated with lung adenocarcinoma subtypes, Ki-67 expression, EGFR mutation and Alk rearrangement [45-47] though there are also negative results in other studies [48]. The measurement of SUVmax and other commonly used factors in lung carcinoma diagnosis such as metabolic tumour volume are non-invasive, but these indicators are inefficient because of their neglect of the relationship of two or more voxels. Radiomics, as biomarkers of medical imaging, has overcome above disadvantages and it is promising in clinical practice because of its non-invasive characteristic and routine employment in clinical. It has become possible that imaging features could be applied for disease diagnosis and prognosis [49-52]. For example, Lee and Cui [53] have confirmed the prognostic value of the pleural contact index, an imaging marker, on large-scale, multiple independent stage I NSCLC cohorts with gene expression data.

Studies have shown that colour may be a good image traits in addition to texture [21-24], but to the best of our knowledge, no study has used colour features of medical images for detecting NSCLC so far. In our study, RGB colour space features and HSV colour space features were quantified from merged PET-CT images. For RGB colour space, histograms with 256 bins were generated for Red, Green and Blue channels respectively. The pixel counts (mean, variance) were described for each colour channel according to the colour histograms, and the red mean, red variance, green mean, green variance, blue mean, blue variance were adopted as the RGB colour features in our study. For HSV colour features, the non-uniform quantization of the H, S, and V channels was made. The hue (H) channel was divided into 7 divisions, saturation (S) was divided into 2 divisions, and the brightness (V) was divided into 2 divisions. According to the above quantization, the three colour components (H, S, and V) were combined into one dimensional feature vector L with a 28-bin colour histogram. The pixel counts for these 28 bins were adopted as HSV colour features after normalization.

Studies have indicated that radiomics probes biologic mechanisms because significant association has been found between imaging features and gene-expression patterns [7, 54]. However, the clinical application of visual representation is still controversial because of its

unclear association with other radiomic data such as metabolic information and morphological characteristics of lesions, so the correlation between them should be verified. In our study, we evaluated the correlation between texture features, colour features and other commonly used diagnostic factors such as SUVmax and nodule size [55-57] to evaluate clinical significance of these features. The moderate association was found between them and it indicated the practical value of these features for characterizing tumours. It was interesting to observe that the discriminative features for differentiation between ADC and SqCC were all correlated to SUVmax or tumour size, which verified the positive relation between medical imaging traits and traditional radiomic data.

In our study, we also compared age and gender difference between the two groups because previous studies have found that SqCC presented a higher proportion of men, a higher age than ADC patients [58], which indicated that age and gender were relevant factors to tumor subtypes. In our study, it was verified that there was a significant difference in age and gender distribution for NSCLC subtypes.

Some previous studies have shown that combining texture and colour features could result in better detection performance in esophageal cancer [32, 52]. We conducted our experiment on NSCLC with texture and colour features to see if it could achieve good classification results. Our study showed that features combining texture and colour performed best with AUC of 0.89 (95% CI, 0.78 to 1.00), colour features got an AUC of 0.85 (95% CI, 0.71 to 0.99) and texture features got an AUC of 0.68 (95% CI, 0.48 to 0.88). It verified the hypothesis that colour features play a key role in discriminating NSCLC subtypes [59].

Our study has some limitations. The sample size in our study was not large. However, the samples were collected from two independent cohorts and it could reduce selection bias and avoid over-fitting. It may be helpful for the versatile application of the results because two sources of images would better represent the imaging variation expected in clinical practice [60]. Besides, the regions of interest were drawn manually. In later research, automated method should be applied to eliminate intra- and inter-observer variation.

In summary, the positive relationship between texture features, colour features and other factors such as SUVmax and tumour size has been verified. The colour features are promising in NSCLC subtype differentiation and the features combining texture and colour of PET-CT images could result in better classification performance.

Acknowledgements

This study has received funding by the National Natural Science Foundation of China (81773542/ 81530087). We acknowledge radiologists at Xuanwu Hospital Capital Medical University in China and Cork University Hospital in Ireland (CUH) for their support acquiring the pilot patient data.

References

[1] Travis WD, Brambilla E, Nicholson AG, et al (2015) The 2015 World Health Organization classification of lung tumours: impact of genetic, clinical and radiologic advances since the 2004 classification. J Thorac Oncol 10: 1243-1260.

[2] Travis WD, Brambilla E, Burke AP, Marx A, Nicholson AG (2015) Introduction to the 2015 World Health Organization classification of tumours of the lung, pleura, thymus, and heart. J Thorac Oncol 10: 1240-1242.

[3] Schuurbiers OCJ, Meijer TWH, Kaanders JHAM, et al (2014) Glucose metabolism in NSCLC is histology-specific and diverges the prognostic potential of 18 FDG-PET for adenocarcinoma and squamous cell carcinoma. J Thorac Oncol 9: 1485-1493.

[4] Meijer, TW, Schuurbiers OC, Kaanders JH, et al (2012) Differences in metabolism between adeno-and squamous cell non-small cell lung carcinomas: spatial distribution and prognostic value of GLUT1 and MCT4. Lung Cancer 76: 316-323.

[5] Stella GM, Luisetti M, Pozzi E, Comoglio PM (2013) Oncogenes in non-small-cell lung cancer: emerging connections and novel therapeutic dynamics. Lancet Respir Med 1: 251-261.

[6] Shtivelman E, Hensing T, Simon GR et al (2014) Molecular pathways and therapeutic targets in lung cancer. Oncotarget 5: 1392-1433.

[7] Aerts HJ, Velazquez ER, Leijenaar RT, et al (2014) Decoding tumour phenotype by noninvasive imaging using a quantitative radiomics approach. Nat Commun 5:4006.

[8] Lambin P, Rios-Velazquez E, Leijenaar R, et al (2012). Radiomics: extracting more information from medical images using advanced feature analysis. European journal of cancer 48(4): 441-446.

[9] Gillies RJ, Kinahan PE, Hricak H (2015) Radiomics: images are more than pictures, they are data. Radiology 278: 563-577.

[10] Hatt M, Tixier F, Pierce L, Kinahan PE, Rest CCL, Visvikis D (2017) Characterization of PET-CT images using texture analysis: the past, the present… any future? Eur J Nucl Med Mol I 44: 151-165.

[11] Chan SC, Cheng NM, Hsieh CH, et al (2017) Multiparametric imaging using FDG PET-CT heterogeneity parameters and functional MRI techniques: prognostic significance in patients with primary advanced oropharyngeal or hypopharyngeal squamous cell carcinoma treated with chemoradiotherapy. Oncotarget 8: 62606-62621.

[12] Chicklore S, Goh V, Siddique M, Roy A, Marsden PK, Cook GJR (2013) Quantifying tumour heterogeneity in FDG PET-CT imaging by texture analysis. Eur J Nucl Med Mol I 40: 133-140.

[13] Jia W, Gensheimer MF, Dong X, et al (2016) Robust Intratumor Partitioning to Identify High-Risk Subregions in

Lung Cancer: A Pilot Study. International Journal of Radiation Oncology Biology Physics 95:1504-1512

[14] Parmar C, Leijenaar RT, Grossmann P et al (2015) Radiomic feature clusters and prognostic signatures specific for lung and head & neck cancer. Sci Rep-UK 5: 11044.

[15] ER A, Varma S, Paul V (2017) Classification of Brain MR Images using Texture Feature Extraction. IJCSE 5: 1722-1729.

[16] Wolsztynski E, Mou T, O'Regan K et al (2017) Model and texture-based characterizations of intratumoural heterogeneity in FDG-PET imaging of lung cancer. J Nucl Med 58: 148-148.

[17] Lee SJ, Zea R, Kim DH, Lubner MG, Deming DA, Pickhardt PJ (2017) CT texture features of liver parenchyma for predicting development of metastatic disease and overall survival in patients with colourectal cancer. Eur Radiol 2017: 1-9.

[18] Wu J, Aguilera T, Shultz D, et al (2016) Early-Stage Non-Small Cell Lung Cancer: Quantitative Imaging Characteristics of (18)F Fluorodeoxyglucose PET/CT Allow Prediction of Distant Metastasis. Radiology 28:151829.

[19] Wu W, Parmar C, Grossmann P, et al (2016) Exploratory study to identify radiomics classifiers for lung cancer histology. Front Oncol 6: 71.

[20] Liu Y, Kim J, Balagurunathan Y, et al (2016) Radiomic features are associated with EGFR mutation status in lung adenocarcinomas. Clin lung cancer 17: 441-448.

[21] Vieira PM, Ramos J, Lima CS (2015) Automatic detection of small bowel tumours in endoscopic capsule images by ROI selection based on discarded lightness information. IEEE 2015: 3025-3028.

[22] Suman S, Malik AS, Riegler M, et al (2017) Detection and Classification of Bleeding Region in WCE Images using Colour Feature. Proceedings of the 15th International Workshop on Content-Based Multimedia Indexing. ACM 2017: 17.

[23] Zhang D, Zhang H, Zhang B (2017) Tongue Colour Analysis for Medical Application. Tongue Image Analysis. Springer, Singapore 2017: 207-223.

[24] Van der Sommen F, Zinger S, Curvers WL, et al (2016) Computer-aided detection of early neoplastic lesions in Barrett's esophagus. Endoscopy 48: 617-624.

[25] Hatt M, Majdoub M, Valli ères M et al (2015) FDG PET uptake characterization through texture analysis: investigating the complementary nature of heterogeneity and functional tumour volume in a multi–cancer site patient cohort. J Nucl Med 56: 38-44.

[26] Luo X, Zang X, Yang L et al (2017) Comprehensive Computational Pathological Image Analysis Predicts Lung Cancer Prognosis. J Thorac Oncol 12: 501-509.

[27] Hughes NM, Mou T, O'Regan KN, et al (2016) Prognostic value of tumour heterogeneity evaluated by FDG-PET-CT imaging in lung cancer patients. J Clin Oncol 2016: 11564-11564.

[28] Haralick RM, Shanmugam K (1973) Textural features for image classification. IEEE T Syst Man Cy-S 1973: 610-621.

[29] Xie T, Chen X, Fang J et al (2017) Textural features of dynamic contrast-enhanced MRI derived model- free and model-based parameter maps in glioma grading. J Magn Reson Imaging. DOI: 10.1002/jmri.25835.

[30] Weszka J S, Dyer C R, Rosenfeld A (1976) A Comparative Study of Texture Measures for Terrain Classification. IEEE Transactions on Sytems Man & Cybernetics, 6:269-285.

[31] Xia DS, Jin S, Wang J (1999) Fractal dimension and GGCM based meteorology cloud pictures recognition description of texture complexity and roughness by fractal dimension. Journal of Nanjing University of Science and Technology, 23:278-281. (in Chinese)

[32] Freitas NR, Vieira PM, Lima E, Lima CS (2017) Using cystoscopy to segment bladder tumours with a multivariate approach in different colour spaces. IEEE 2017: 656-659.

[33] Zhu YM, Nortmann CA (2011) Pixel-feature hybrid fusion for PET/CT images. Journal of digital imaging 24: 50-57.

[34] Nakanishi K, Ohsaki Y, Kurihara M, et al (2007) Colour auto-fluorescence from cancer lesions: improved detection of central type lung cancer. Lung Cancer 58: 214-219.

[35] Bora DJ, Gupta AK, Khan FA (2015) Comparing the performance of L* A* B* and HSV colour spaces with respect to colour image segmentation. IJETAE 5: 192-203.

[36] Ford A, Roberts A (1998) Color space conversions. Westminster University, London 1998: 1-31.

[37] Kodituwakku S R, Selvarajah S (2004). Comparison of color features for image retrieval. Indian Journal of Computer Science and Engineering 1: 207-211.

[38] Sural S, Qian G, Pramanik S (2002) Segmentation and histogram generation using the HSV colour space for image retrieval[C]//Image Processing. 2002. Proceedings. 2002 International Conference on. IEEE 2: II-II.

[39] Cantrell K, Erenas M M, de Orbe-Pay á I, et al (2009) Use of the hue parameter of the hue, saturation, value colour space as a quantitative analytical parameter for bitonal optical sensors. Analytical chemistry 82: 531-542.

[40] Song J M, Kim H J. Colour space quantization descriptor structure: U.S. Patent 6,850,639[P]. 2005-2-1.

[41] Luo W, Li H (2012) Dominant Colour Retrieval of Wood Image Based on Non Equal Interval Quantization of Colour Space. Journal of Northeast Forestry University 40:159-162.

[42] Setio AAA, Van Der Sommen F, Zinger S, Schoon EJ, De With PHN (2013) Evaluation and Comparison of Textural Feature Representation for the Detection of Early Stage Cancer in Endoscopy. VISAPP (1). 2013: 238-243.

[43] Wang XY, Zhao YF, Liu Y, Yang YK, Wu N (2017) Prognostic value of metabolic variables of [18F] FDG PET-CT in surgically resected stage I lung adenocarcinoma. Medicine. 96: 7941.

[44] Lim C, Sekhon H, Cutz J et al (2017) Improving molecular testing and personalized medicine in non-small-cell lung cancer in Ontario. Curr Oncol 24: 103.

[45] Vesselle H, Salskov A, Turcotte E et al (2008) Relationship between non-small cell lung cancer FDG uptake at PET, tumour histology, and Ki-67 proliferation index. J Thorac Oncol 3: 971-978.

[46] Choi H, Paeng JC, Kim DW et al (2013) Metabolic and metastatic characteristics of ALK-rearranged lung adenocarcinoma on FDG PET-CT. Lung Cancer 79: 242-247.

[47] Moscoso A, Ruibal Á, Dom ńguez-Prado I, et al (2018) Texture analysis of high-resolution dedicated breast FDG

PET images correlates with immunohistochemical factors and subtype of breast cancer. Eur J Nucl Med Mol I 45: 196-206.

[48] Putora PM, FrühJ M, Müller J (2013) FDG-PET SUV-max values do not correlate with epidermal growth factor receptor mutation status in lung adenocarcinoma. Respirology 18: 734-735.

[49] Tixier F, Le Rest CC, Hatt M et al (2011) Intratumour heterogeneity characterized by textural features on baseline FDG PET images predicts response to concomitant radiochemotherapy in esophageal cancer. J Nucl Med 52: 369-378.

[50] Eskreis-Winkler S, Zhang Y, Zhang J, Liu Z, Dimov A, Gupta A, Wang Y (2017) The clinical utility of QSM: disease diagnosis, medical management, and surgical planning. NMR in Biomed 30:-.

[51] Zhang M, Yang Y, Shen F, Zhang HW, Wang Y (2017) Multi-view feature selection and classification for Alzheimer's Disease diagnosis. Multimed Tools Appl 76: 10761-10775.

[52] Van Der Sommen F, Zinger S, Schoon EJ, De With PHN (2014) Supportive automatic annotation of early esophageal cancer using local gabor and colour features. Neurocomputing 144: 92-106.

[53] Lee J, Cui Y, Sun X, et al (2017) Prognostic value and molecular correlates of a CT image-based quantitative pleural contact index in early stage NSCLC. European Radiology 28:1-11.

[54] Starmans M, Lieuwes N, Span P et al (2012) Independent and functional validation of a multi-tumour-type proliferation signature. Brit J Cancer 107: 508-515.

[55] Ko JP, Berman EJ, Kaur M et al (2012) Pulmonary Nodules: growth rate assessment in patients by using serial CT and three-dimensional volumetry. Radiology 262: 662-671.

[56] Henschke CI, Yankelevitz DF, Yip R et al (2012) Lung cancers diagnosed at annual CT screening: volume doubling times. Radiology 263: 578-583.

[57] Wilson DO, Ryan A, Fuhrman C et al (2012) Doubling times and CT screen–detected lung cancers in the Pittsburgh Lung Screening Study. Am J Resp Crit Care 185: 85-89.

[58] Ha S, Choi H, Cheon GJ et al (2014) Autoclustering of non-small cell lung carcinoma subtypes on FDG PET using texture analysis: a preliminary result. Nucl Med Mol Imaging. 48: 278-286.

[59] Wu H, Sun T, Wang J et al (2013) Combination of radiological and gray level co-occurrence matrix textural features used to distinguish solitary pulmonary nodules by computed tomography. J Digit Imaging 26: 797-802.

[60] Van der Sommen F, Zinger S, Curvers WL et al (2016) Computer-aided detection of early neoplastic lesions in Barrett's esophagus. Endoscopy 48: 617-24.